

Architecture Specific Generation of Large Scale Lattice Boltzmann Methods for Sparse Complex Geometries

Journal Title
XX(X):1–16
©The Author(s) 2016
Reprints and permission:
sagepub.co.uk/journalsPermissions.nav
DOI: 10.1177/ToBeAssigned
www.sagepub.com/

SAGE

Philipp Suffa¹, Markus Holzer², Harald Köstler^{1,3} and Ulrich Rüde^{1,2}

Abstract

We implement and analyse a sparse / indirect-addressing data structure for the Lattice Boltzmann Method to support efficient compute kernels for fluid dynamics problems with a high number of non-fluid nodes in the domain, such as in porous media flows. The data structure is integrated into a code generation pipeline to enable sparse Lattice Boltzmann Methods with a variety of stencils and collision operators and to generate efficient code for kernels for CPU as well as for AMD and NVIDIA accelerator cards. We optimize these sparse kernels with an in-place streaming pattern to save memory accesses and memory consumption and we implement a communication hiding technique to prove scalability. We present single GPU performance results with up to 99% of maximal bandwidth utilization. We integrate the optimized generated kernels in the high performance framework WALBERLA and achieve a scaling efficiency of at least 82% on up to 1024 NVIDIA A100 GPUs and up to 4096 AMD MI250X GPUs on modern HPC systems. Further, we set up three different applications to test the sparse data structure for realistic demonstrator problems. We show performance results for flow through porous media, free flow over a particle bed, and blood flow in a coronary artery. We achieve a maximal performance speed-up of 2 and a significantly reduced memory consumption by up to 75% with the sparse / indirect-addressing data structure compared to the direct-addressing data structure for these applications.

Keywords

Sparse Lattice Boltzmann Method, Indirect Addressing, Complex Geometries, High Performance Computing, GPU computing, Large Scale, Porous Media

Introduction

The increasing power of high-performance computing (HPC) systems enables computational fluid dynamic (CFD) simulations, which were still out of scope some years ago. The leading HPC systems in the Top500 list¹ reach a peak performance of ExaFLOPs, so they can perform 10^{18} floating point operations per second. This trend is also caused by the utilization of accelerators, such as NVIDIA, AMD, or INTEL Graphics Processing Units (GPUs). With these new computing capabilities, computational fluid dynamic (CFD) problems, which were out of scope before, can now be tackled, such as fully resolved porous media simulations at relevant scales, as presented in [Mattila et al. \(2016\)](#) or entire body arterial flows as in [Randles et al. \(2015\)](#). However, it is not trivial to fully utilize the maximum performance of these HPC systems, especially for systems with accelerators ([Brodtkorb et al. \(2013\)](#), [Hijma et al. \(2023\)](#), [Lai et al. \(2020\)](#), [Rak \(2024\)](#)).

The Lattice Boltzmann method (LBM) ([Chen and Doolen \(1998\)](#), [Krüger et al. \(2017\)](#)) is an efficient inherently parallel method to solve CFD problems for complex geometries. On many HPC systems, the LBM shows excellent performance as presented in [Liu et al. \(2023\)](#), [Spinelli et al. \(2023\)](#), [Watanabe and Hu \(2022\)](#) or [Godenschwager et al. \(2013\)](#).

There are two common ways to store data for LBM simulations. The direct-addressing LBM stores and computes all cells of the domain. We call this technique "dense" or "direct-addressing" data structure in the following. It is shown to be very fast and efficient for

most simulation setups (see [Kummerländer et al. \(2023\)](#), [Lehmann et al. \(2022\)](#) and [Latt et al. \(2021\)](#)). However, it struggles in performance and memory consumption for simulation domains with a high number of non-fluid nodes, such as in porous media flows. In the following, we call such domains "sparse domains". In contrast, simulations with a high percentage of fluid nodes, such as a free channel flow, we will refer to as "dense domain".

The second way to store data for LBM simulations is the indirect-addressing storage format. We call it "sparse" data structure in the following. This approach stores only fluid cells and can therefore save a significant amount of memory. Additionally, the sparse approach reaches superior performance for sparse complex geometries as compared with the dense approach. In this sense, the sparse approach has been found to be very efficient, see e.g. in [Wittmann et al. \(2013\)](#) and [Schulz et al. \(2002\)](#). In particular, the sparse data structure is employed successfully to simulate porous media

¹Chair for System Simulation, Friedrich Alexander Universität Erlangen-Nürnberg, Erlangen, Germany

²Parallel Algorithm Team, CERFACS, Toulouse, France

³Erlangen National High Performance Computing Center (NHR@FAU), Erlangen, Germany

Corresponding author:

Email: philipp.suffa@fau.de

flows as in Pan et al. (2004), Zeiser et al. (2009), Wang et al. (2005) and Vidal et al. (2010).

In this work we study the code generation for highly efficient LBMs and their performance on large HPC systems. The sparse data structure is realised with the code generation framework of *lbmpy* (Bauer et al. (2021)), allowing it to run on a variety of architectures, such as all common CPUs as well as NVIDIA and AMD accelerators. The generated sparse compute kernels are integrated in the multiphysics HPC framework WALBERLA (Bauer et al. (2020)) to enable massively parallel simulations with excellent scalability (Holzer et al. (2024)).

We compare the performance of the generated sparse kernels with the dense approach and present the scaling performance of the sparse data structure on modern HPC systems such as JUWELS Booster (Alvarez (2021)) and LUMI². Further, we show performance results for realistic model problems such as a flow in a porous media, a flow over a packed bed, and a coronary artery flow on a high number of accelerator cards.

Lattice Boltzmann Method

The lattice Boltzmann method is a mesoscopic method established as an alternative to classical Navier-Stokes solvers (Krüger et al. (2017)). The simulation domain is usually discretized by a lattice of square cells. A cell at position \mathbf{x} stores a particle distribution function (PDF) $f_i(\mathbf{x}, t)$, which represents the probability of particles at time t with discrete velocity \mathbf{c}_i . The macroscopic quantities, lattice density ρ and momentum density $\rho\mathbf{u}$, can be computed from the PDFs using

$$\rho(\mathbf{x}, t) = \sum_i f_i(\mathbf{x}, t) \quad \text{and} \quad \rho\mathbf{u}(\mathbf{x}, t) = \sum_i \mathbf{c}_i f_i(\mathbf{x}, t). \quad (1)$$

A standard set of discrete three-dimensional velocity directions would be the D3Q19 stencil, which results in $Q = |\{\mathbf{c}_i\}| = 19$ PDFs, respectively.

The Boltzmann equation discretized in time, space, and velocity space reads

$$f_i(\mathbf{x} + \mathbf{c}_i\Delta t, t + \Delta t) = f_i(\mathbf{x}, t) + \Omega_i(\mathbf{x}, t), \quad (2)$$

with Δx as lattice spacing, Δt as time step size and Ω as collision operator. The LB equation can be separated into a collision step

$$\tilde{f}_i(\mathbf{x}, t) = f_i(\mathbf{x}, t) + \Omega_i(\mathbf{x}, t) \quad (3)$$

and a streaming step

$$f_i(\mathbf{x} + \mathbf{c}_i\Delta t, t + \Delta t) = \tilde{f}_i(\mathbf{x}, t), \quad (4)$$

with \tilde{f}_i denoting the post-collision state of the PDFs.

The simplest collision operator is the single relaxation time (SRT) operator

$$\Omega_i^{\text{SRT}}(f) = -\frac{f_i - f_i^{\text{eq}}}{\tau} \Delta t, \quad (5)$$

which relaxes the PDFs towards the equilibrium f_i^{eq} determined by the relaxation time τ . The equilibrium is given

by

$$f_i^{\text{eq}}(\mathbf{x}, t) = w_i \rho \left(1 + \frac{\mathbf{u} \cdot \mathbf{c}_i}{c_s^2} + \frac{(\mathbf{u} \cdot \mathbf{c}_i)^2}{2c_s^4} - \frac{\mathbf{u} \cdot \mathbf{u}}{2c_s^2} \right) \quad (6)$$

with the speed of sound $c_s^2 = (1/3)\Delta x^2/\Delta t^2$ and velocity set specific weights w_i . The fluid velocity of a cell at position \mathbf{x} is calculated as $\mathbf{u}(\mathbf{x}, t) = \rho\mathbf{u}(\mathbf{x}, t)/\rho(\mathbf{x}, t)$. The kinematic viscosity ν is related to the relaxation time τ and the dimensionless relaxation parameter $\omega = \frac{\Delta t}{\tau} \in]0, 2[$ by

$$\nu = c_s^2 \left(\frac{\tau}{\Delta t} - \frac{1}{2} \right) = c_s^2 \left(\frac{1}{\omega} - \frac{1}{2} \right). \quad (7)$$

Data Structures in WALBERLA

In the WALBERLA framework, the simulation domain is partitioned into uniform cubic blocks, typically with a size of around 64^3 cells on CPUs and about 256^3 cells on GPUs. In Figure 1 the block partitioning into uniform cubic blocks is shown. For parts of the domain where no fluid is present, blocks that only consist of obstacle cells can be discarded. The remaining blocks are then distributed to the available MPI processes, so that every process gets at least one block. However, more blocks per process are also possible and can be useful, for example, when load balancing is necessary, as we will see in the following. The organization of a computational grid into blocks introduces a hierarchy that is found essential for efficient processing on the extreme scale since many operations can be better organized in such a hierarchy. In particular, performing the mesh partitioning and load balancing in terms of blocks keeps the complexity and overhead of these algorithms small (see Schornbaum and Rüde (2016) and Schornbaum and Rüde (2018)).

As indicated in Figure 1, the dense / direct-addressing data structure implemented in WALBERLA stores the PDFs for every cell in memory, even for non-fluid cells. However, for sparse domains or porous media flows, the porosity

$$\phi = \frac{N_F}{N} \quad (8)$$

with N as the total number of cells and N_F as the number of fluid cells, can be arbitrarily small. Therefore, much memory may be wasted by storing non-fluid cells on these blocks. Furthermore, a branch statement in the LBM kernel is needed to check, if the current cell is a fluid or an obstacle cell. Additionally, non-fluid cells can cause unnecessary memory traffic, when cache lines contain fluid and non-fluid cells, and hardware prefetchers may read data from non-fluid cells, which is not used. Especially when the domain is sparse, the dense approach creates a significant overhead and can lead to a significant performance loss (Godenschwager et al. (2013)).

Sparse Data Structure

To avoid the disadvantages of the dense data structure, we have developed a sparse data structure in WALBERLA and *lbmpy*. This technique is also used by other LBM frameworks such as HARVEY (Randles et al. (2013)), Musubi (Hasert et al. (2014)), ILBDC (Zeiser et al. (2009)) and MUPHY (Bernaschi et al. (2008)), just to mention a few.

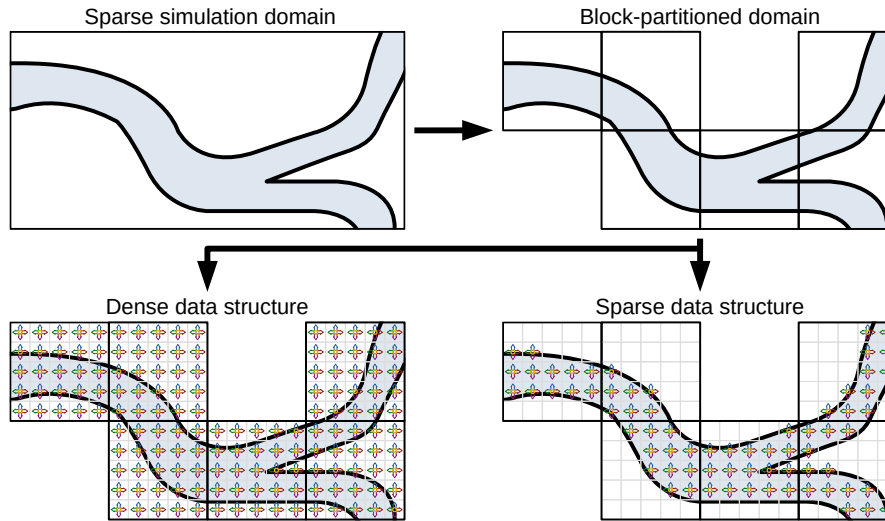


Figure 1. Exemplary setup of a sparse simulation domain in 2D with a low percentage of fluid covering the domain (light blue), and a high number of obstacle cells. Visualisation of the block partitioning with extraction of blocks without fluid. Illustration of a dense and a sparse data structure for an exemplary setup of 5x5 cells per block and a D2Q5 stencil. While the dense data structure stores PDFs and operates on all cells, the sparse data structure only stores and operates on fluid cells.

The idea is to only store fluid cells in a one-dimensional array, we call `PDF-list`, so that no memory is wasted on storing non-fluid cells. Furthermore, with such a data structure LBM kernels only have to iterate over fluid cells, and no branch conditions are needed in the innermost kernel loops. On the other hand, one loses spatial information when storing cell data in a linear array only. With the direct-addressing data structure, PDFs can easily be accessed by their spatial location \mathbf{x} and the PDF index i . This access via index arithmetic is not possible for the sparse `PDF-list`.

A second data structure, the `index-list`, is introduced to recover the lost spatial information. This list stores the streaming information from one PDF to another. So for one PDF, the `index-list` stores the location of the PDF, to which it will propagate to in the streaming step. Using the `index-list`, we can access the neighbors of a cell using one indirection. Therefore, this approach is called an indirect-addressing scheme.

While the `PDF-list` consists of $N_F \cdot Q$ entries, where Q is the size of the stencil, the `index-list` only consists of $N_F \cdot (Q - 1)$ entries, since the center PDF need not to be stored, as no propagation information is needed for the center PDF.

The exact structure of the `PDF-list` and `index-list` is illustrated in [Figure 2a](#) and [Figure 2b](#), respectively. We show the `PDF-list` in a Structure-of-Array (SoA) format, so all PDFs of one direction lie next to each other in memory. The demonstrator domain consists of fluid cells (white), no-slip boundary cells, which indicate an obstacle (grey), velocity bounce back boundary conditions (blue) and ghost layer cells, which are needed for the communication between blocks (light yellow).

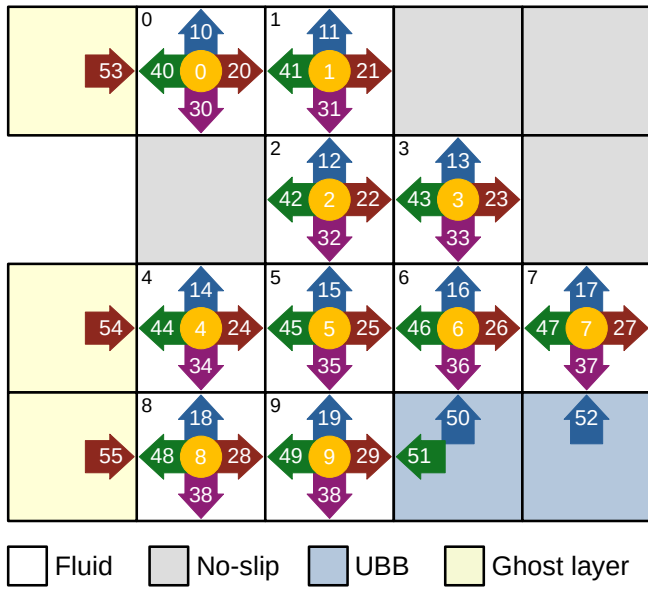
In [Figure 2a](#) the PDF of cell 0 in direction west (PDF_w^0) is stored at position 40 in the `PDF-list`, and the PDF_w^1 of cell 1 is stored at position 41. To perform a streaming step for PDF_w^0 in cell 0, we have to look up the pull index (for a presumed pull-streaming pattern) in the `index-list`. This is illustrated in [Figure 2b](#), where the pull index of the PDF_w^0

is the PDF 41. This makes sense, as for direction west we pull PDF_w from the right neighbour cell. The pull index look-up in the `index-list` is done for all PDFs of all fluid cells to perform a complete streaming step. The actual layout of the `PDF-list` and `index-list` in memory is illustrated in [Figure 2c](#). There the SoA layout is used.

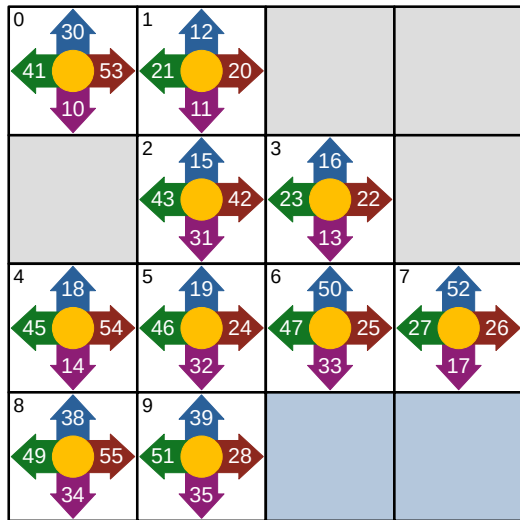
Sparse Boundary Conditions Some modifications to the list data structures are made to support the implementation of boundary conditions. No-slip boundary conditions can easily be realised by setting the pull indices of the PDF, which would pull from a no-slip boundary to the inverse direction of the PDF. This is also illustrated in [Figure 2b](#). For illustration we focus on PDF_w^1 of cell 1. It would pull from its right neighbour cell, but this is an obstacle (no-slip) cell. So PDF_w^1 (PDF 41) pulls from the PDF in east direction of its same cell 1, which is then the PDF_e^1 with index 21. Also, periodic boundary conditions are easy to implement; here, the pull index of the PDF, which must stream from the periodic boundary on the opposite side, is just set to the PDF on the other side of the domain.

For boundary conditions other than no-slip or periodic, PDFs, which correspond to a boundary cell but point to a fluid cell, must be appended to the `PDF-list`. Further, the `index-list` has to be modified, so that PDFs of fluid cells next to boundary cells pull from the boundary PDF cells. This is also illustrated for velocity-bounce-back boundary conditions (UBB) in [Figure 2](#). Here, the PDF_w^9 (PDF 49, cell 9, direction west) pulls from PDF_w of the UBB boundary cell right next to it, which is the appended PDF with index 51.

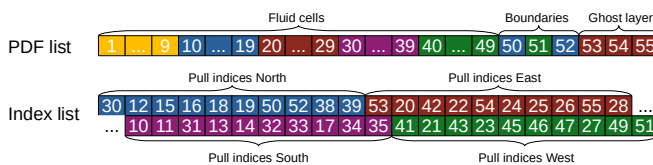
Sparse Communication For the dense data structure, every block has a ghost layer of at least one cell all around in which it stores the PDFs traveling in the corresponding direction. This ghost layer is used to communicate PDF information between MPI processes. For the communication between sparse blocks, we also have to append these ghost layer PDFs to the `PDF-list` and modify the `index-list` so that



(a) PDF-list in SoA layout with appended PDFs from velocity-bounce-back (UBB) boundaries (in light blue) and ghost layers (in light yellow). The numbers indicate the position of the PDF in the PDF-list.



(b) Structure of the index-list for the corresponding PDF-list in Figure 2a. The numbers indicate from which position in the PDF-list to pull from in the streaming step.



(c) Actual structure of PDF-list and index-list, as they lie in memory in SoA layout.

Figure 2. Structure of the PDF-list and the index-list for an exemplary D2Q5 velocity set. The domain contains fluid cells (white), ghost layers (light yellow), velocity-bounce-back (UBB) boundaries (light blue) and no-slip boundaries (grey). The directions of the PDF stencil are indicated by colors as well. In direction west there is a MPI interface to the neighboring block considered. North, east and south cells next to the presented cells are also considered as no-slip cells.

cells next to the MPI interface pull from these ghost layer PDFs (see Figure 2 yellow cells).

Nevertheless, as we only append boundary and ghost-layer PDFs pointing to fluid, the memory overhead of the additionally stored PDFs is relatively low. In LBM kernels, we still only need to iterate over fluid cells.

Code Generation for Sparse Kernels

Many variants of the LBM have been developed over the last decades, which vary in complexity, accuracy, and computational cost. The code generation framework *lbmpy* is capable to generate kernels for most of these LBMs. It supports a wide range of velocity sets, for example, the D2Q5, D2Q9, D3Q15, D3Q19, D3Q27, and more. Further, highly efficient code for different collision operators can be generated. For example, the classical collision models such as single-relaxation time (SRT), two-relaxation time (TRT), and multi-relaxation time (MRT) operators (Krüger et al. (2017)) are available. However, more advanced collision models are also supported, such as the central moment operator or the cumulant operator. The cumulant LBM, e.g., provides superior accuracy and stability for high Reynolds number flows (see Geier et al. (2015)). The complexity of the collision models increases from the SRT model to the cumulant model in terms of complexity and the number of moment transfers, so e.g. the transfer from moment space to central moment space or to cumulant space. This can increase the number of floating point operations in the collision step significantly. However, due to optimizations such as common sub-expression elimination (CSE), the number of operations per cell lies between only 200 and 400 FLOPS for a D3Q19 stencil irrespective of the collision model (Hennig et al. (2022)). Therefore, the performance of the compute kernels remains memory-bound, as the number of memory accesses stays constant for all collision operators. Consequently, we can report a similar performance for all collision operators in the following in Figure 8.

Additionally, *lbmpy* provides a generic development tool to design new collision schemes. The high-level domain-specific language of *lbmpy* allows the user to formulate, extend, and test various Lattice Boltzmann Methods (Bauer et al. (2021)).

To profit from the functionalities of the code generation pipeline *lbmpy*, we integrated the generation of new sparse LBM kernels, boundary handling kernels, and communication kernels. All together, we are now able to generate efficient sparse kernels for various velocity sets and collision operators, which can run on all common CPUs and NVIDIA and AMD GPUs.

In Figure 3, the code generation pipeline is presented. In the model creation, the user defines the LB method by choosing a specific collision model, a stencil and a streaming pattern. Further, a force model, the option of storing the PDFs in a zero-centered storage fashion, or similar can be set. After defining the model, the LB method is represented as a set of equations stored in an abstract syntax tree (AST). This AST is now passed to *pystencils* (Bauer et al. (2019)), which can perform further optimizations, such as common subexpression elimination, loop splitting, or adding vector intrinsics for single-instruction-multiple-data (SIMD)

execution. At this point, we have to decide about the data structure of the generated kernels to be sparse or dense, which defines the loop nest of the generated code and the data accesses. To support a complete CFD application, the generation of LB kernels, as well as boundary and communication kernels, is needed. The code generation pipeline supports all of the kernels for the sparse and the dense data structure. As the last step, the actual code is generated for a specified architecture. In particular, all kernels can be generated in plain C-code to support all common CPUs. However, the kernels can also be generated with a HIP³ or CUDA⁴ API to support the GPU vendors AMD or NVIDIA, respectively. Lastly, these optimized kernels can be run interactively in IPython⁵, but they can also be integrated into a high-performance framework such as WALBERLA to be run in parallel on thousands of CPU or GPU nodes.

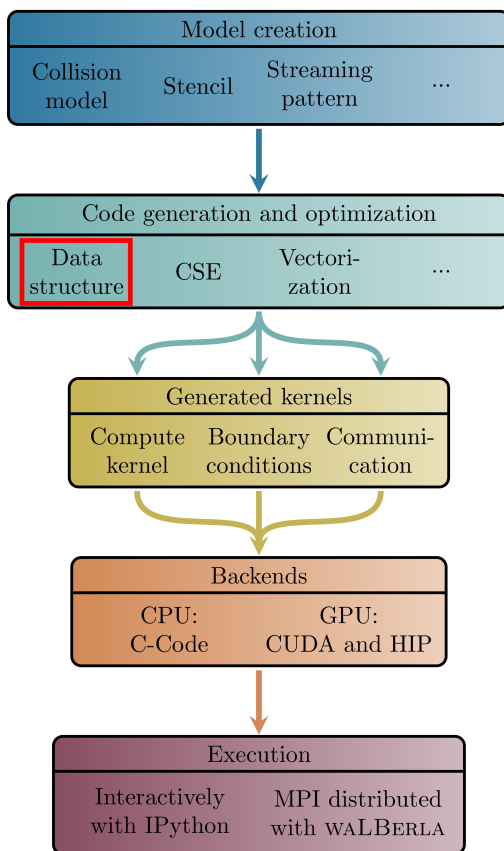


Figure 3. Complete workflow of the code generation pipeline of *lbmpy*. For a full CFD application compute kernels as well as boundary and communication kernels are generated.

Single Node Results In [Figure 4](#), we present the performance of the generated sparse LBM kernel in comparison to the generated direct-addressing kernel. The diagram shows the mega fluid lattice updates per second (MFLUPs) depending on the porosity ϕ as defined in [Equation 8](#). The LB method uses a D3Q19 velocity set and the SRT collision operator. The benchmark measures the LBM kernel performance without boundary handling or communication, and it is performed on a single NVIDIA A100 GPU.

We observe that the single GPU performance of the sparse kernel is quite close to the theoretical peak performance. Furthermore, the MFLUPs performance remains essentially constant for decreasing porosity.

However, [Figure 4](#) also shows that the sparse kernels perform worse for $\phi \geq 0.75$. This is caused by the extra memory accesses of the sparse data structure. A dense kernel has to read and write every PDF of a cell per time step. This results in a memory access volume of $2Q \cdot B_{\text{PDF}}$ bytes per cell on GPUs, with Q as stencil size, here 19, and B_{PDF} as the bytes per stored PDF, here 8 bytes for double precision. The sparse kernel, on the other hand, accesses $2Q \cdot B_{\text{PDF}} + (Q - 1) \cdot B_{\text{idX}}$ bytes per cell, because it needs to read neighboring information from the `index-list`. B_{idX} is the number of bytes per index in the `index-list`, here 4 bytes for an integer.

Nevertheless, the performance for the dense kernel decreases linearly when porosity decreases. The reason for this behavior is that dense kernels in WALBERLA traverse all cells, including the non-fluid cells. This avoids the need for a branch instruction for non-fluid cells, as mentioned before. On the other side, this leads to a linear decrease of the fluid lattice updates per second.

As indicated in [Figure 4](#), the theoretical break-even point for sparse and dense kernels is approximately $\phi \sim 0.75$.

On the same NVIDIA A100 GPU we present a comparison of the memory consumption for a lattice of 256^3 cells in [Figure 5](#). The memory usage is measured with the NVIDIA monitoring tool *nvidia-smi*, showing that the sparse data structure consumes linearly less memory with decreasing porosity. On the other hand, the dense data structure exhibits a constant memory footprint because it stores all cells in the domain, regardless of whether a cell is fluid or boundary. For a porosity of 1.0, where all cells in the domain are fluid, the sparse data structure consumes more memory, since it also has to store the `index-list` in addition to the `PDF-list`. The theoretical memory consumption of the LBM kernels can be calculated as:

$$M_{\text{sparse}} = N_{\text{cells}} \cdot \left(\underbrace{2 \cdot Q \cdot B_{\text{PDF}}}_{\text{PDF-lists}} + \underbrace{(Q - 1) \cdot B_{\text{idX}}}_{\text{index-list}} + \underbrace{5 \cdot B_{\text{PDF}}}_{\text{other fields}} \right) \cdot \phi,$$

$$M_{\text{dense}} = N_{\text{cells}} \cdot \left(\underbrace{2 \cdot Q \cdot B_{\text{PDF}}}_{\text{PDF-field}} + \underbrace{5 \cdot B_{\text{PDF}}}_{\text{other fields}} \right). \quad (9)$$

The additional fields stored are a velocity field (3D), a density field (1D), and a flag field to indicate boundary cells (1D).

We see that for the theoretical as well as for the measured memory footprint, the break-even point of the sparse and dense data structure is at a porosity of around $\phi \sim 0.8$, which is a similar result as for the performance comparison. For a higher porosity, the dense data structure is more suitable in terms of memory consumption, and for a lower porosity, the sparse structure becomes superior.

The measured memory consumption for the sparse as well as for the dense LBM in [Figure 5](#) is close to the theoretical memory consumption, so that there is only a small overhead of less than 10% coming from other data structures than the necessary pure PDF data.

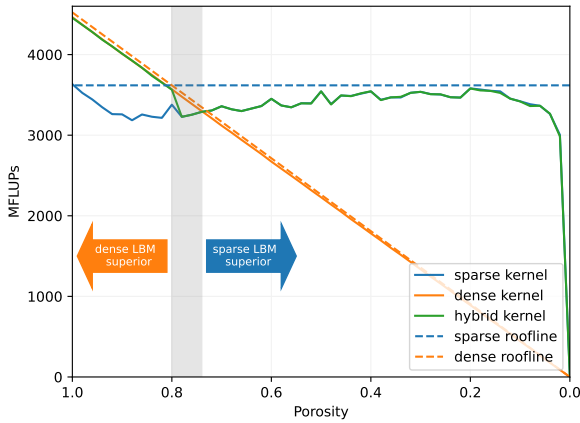


Figure 4. Single GPU benchmark for sparse, dense and hybrid data structure with varying porosity on a NVIDIA A100 with 256^3 cells, D3Q19 velocity set and SRT collision operator. The theoretical performance is calculated from the bandwidth of a streaming benchmark (1361 GB/s) and the theoretical number of memory accesses of the kernels, as LBM code is usually memory bound.

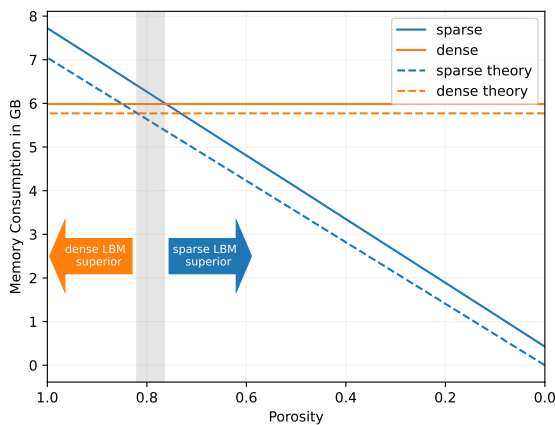


Figure 5. Memory consumption benchmark for 256^3 cells on a single NVIDIA A100 GPU for D3Q19 stencil and pull streaming pattern. The theoretical memory consumption is calculated in Equation 9.

Hybrid Data Structure

In certain application scenarios, a hybrid data structure may be advantageous. As an example, consider a free flow over a particle bed as depicted in Figure 14. After the domain partitioning, some blocks contain only fluid cells, while other blocks consist primarily of non-fluid cells. In this case, neither the sparse nor the dense data structure seems to fit the given scenario perfectly.

Therefore, we implement the hybrid simulations in WALBERLA. From *lbmpy*, sparse and dense LBM and boundary kernels are generated. In WALBERLA, the porosity ϕ is calculated individually on each block to determine the block as a sparse or dense block, based on a porosity threshold ϕ_S . Based on the results in Figure 4 and Figure 5, the porosity threshold should be around $\phi_s \sim 0.8$. During the creation of the data structures on the blocks, a dense

PDF field or a sparse PDF-list and the corresponding index-list is created on the block, and only the corresponding generated sparse or dense kernel runs on the blocks. Besides this functionality, appropriate routines for the communication between sparse and dense blocks must be realized. Again, suitable pack and unpack kernels are generated for CPU or GPU architectures with *lbmpy*, while the MPI communication routine itself stays unchanged.

In Figure 4, we display the performance for the hybrid data structure in green with $\phi_S = 0.8$. As expected, the performance reflects that of the dense kernel for $\phi \geq \phi_S$ and, that of the sparse kernel for $\phi < \phi_S$. Consequently, the hybrid approach can always reach the maximum possible WALBERLA performance per block, independent of the porosity. The same holds for the memory consumption. If we set the porosity threshold to ~ 0.8 as suggested in Figure 5, we also get the best possible memory consumption per block by utilizing the hybrid data structure.

Optimizations to sparse LBM

The high-performance framework WALBERLA in combination with *lbmpy* already provides a wide range of optimizations for LB methods. For the sparse data structure, some of the optimizations had to be adapted or re-implemented. In the following, we specifically describe the implementation of an in-place streaming pattern and a communication hiding technique specially designed for the sparse data structures.

In-place Streaming: AA Pattern

The most common streaming patterns for LBM are the two-grid algorithms, where either PDFs of a cell are pushed into the neighbor cells (push scheme), or PDFs are pulled from the neighbor cells (pull scheme) (Krüger et al. (2017)). These algorithms have in common that a temporary PDF field is needed. This is because PDFs are stored in a different position than where they are read from. As illustrated in Figure 6, these two-grid streaming patterns read from PDF field A, then they propagate (push/pull) the PDFs, and, lastly, they store the propagated results at a different location in the temporary PDF field B. Therefore, these streaming methods are also called AB patterns. After the propagation, a field swap of fields A and B is needed.

The in-place streaming AA pattern on the other hand, enables writing and storing PDF values in the same positions of the PDF field, so that PDFs can be read from field A and also be written to field A without creating data dependencies. This saves the memory of the temporary PDF field B. Additionally, it also saves memory accesses (see Bailey et al. (2009)).

These savings are achieved by introducing two alternating streaming time steps, as shown in Figure 7. In the "odd" time step, PDFs are read from field A and pulled to the current cell. Then, the collision is performed, and the resulting PDFs are pushed back to the neighbor cells to the positions where they were read from on field A. It is worth mentioning, that while we introduced the LBM streaming step as a separate algorithm step in Equation 4, in the actual generated LB kernels streaming and collision is a fused step to save memory accesses. The odd time step consists of two propagations and one collision, and the reads and writes of

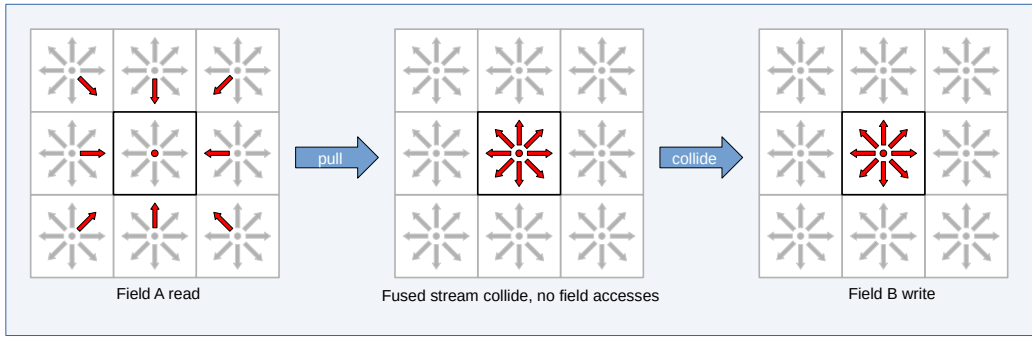


Figure 6. Pull pattern: PDFs are read from field A and, after the fused stream-collide step, they are written to field B.

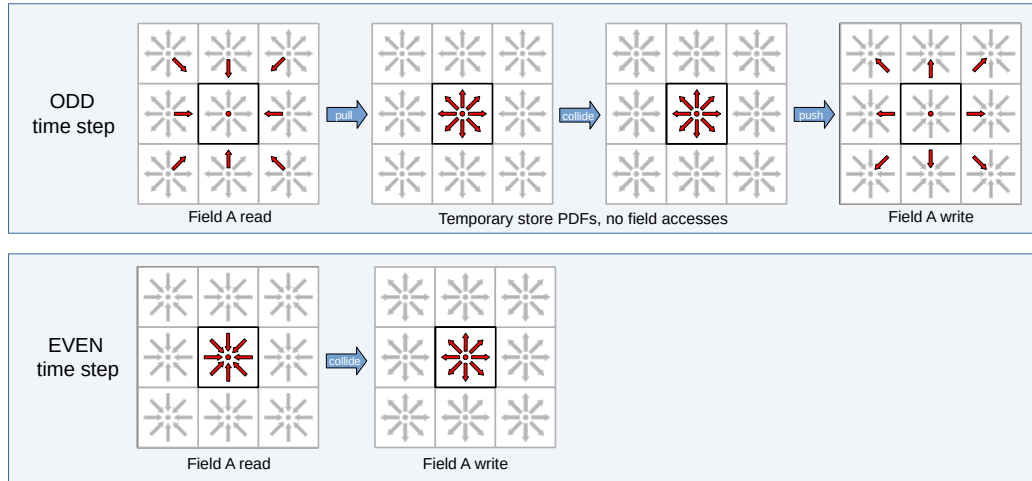


Figure 7. AA pattern: In the “odd” time step, a pull streaming is done, followed by a collision and a push streaming step. As the PDFs are pushed to the same positions as they are read from, the PDFs are stored in the opposite stencil directions. In the “even” time step, only one collision is done, where the PDFs have to be written from the opposite stencil direction to achieve correct macroscopic values. Read and write takes place on the same field, therefore only one PDF field must be stored.

the PDFs take place at the same positions on the same field A. However, this means that after the second propagation, the PDFs are stored in the wrong position of the stencil. Thus we have to take care that PDFs are always in the opposite stencil position after an odd time step. It becomes relevant when we must calculate macroscopic values or when we must communicate with neighbor MPI blocks after an odd time step.

The second time step, the “even” time step, only consists of one collision. The PDFs needed for the collision must be read from the opposite stencil positions to get correct macroscopic value calculations and similar. As there is no propagation in the even time step, no neighboring information is needed there. Consequently, there is also no need to access the pull index list, which saves memory access, as discussed in the following.

After one odd and one even time step, the PDFs are again stored in their right positions, and the outcome is the same as after two push or pull time steps.

The benefit of the AA streaming pattern in terms of memory accesses is shown in [Table 1](#). For the pull pattern in dense kernels, $3Q$ memory accesses are required. One memory access is needed for the read of field A, one is needed for the write on field B, and the third one is a “write allocate B”, which occurs if the data of the PDF of field B is not already stored in the CPU cache, and therefore has

to be loaded into the cache to be written on. A PDF entry is only used once in a fused stream-collide step, and the whole `PDF-list` is unlikely to fit completely in the CPU cache for large-scale runs. Therefore, the “write allocate B” access is mostly present. This memory access only appears on CPUs, as GPUs do not utilize cache structure like CPUs do, so the amount of memory accesses on GPUs per cell is $2Q$. Nevertheless, we want to avoid the third access on CPUs by utilizing an in-place streaming pattern. The data is already in the CPU cache because we read and write on the same PDF positions in the same PDF field. By this, we avoid the cache miss and end up with $2Q$ memory accesses per cell.

For sparse kernels, utilizing the AA pattern has even more advantages in terms of memory access. For the pull pattern, in addition to the `PDF-list`, also the `index-list` has to be read to get the pull accesses for the propagation step, which adds a $(Q - 1)$ to our count of memory accesses. In total, we need $3 \cdot Q + (Q - 1)$ memory accesses for sparse LBM kernels with the pull streaming pattern.

For the AA pattern on the other side, we only need neighboring information in every second (odd) time step because on even time steps, we only compute cell-local, and therefore no neighboring information is needed. So, the memory accesses for the index list can be halved to $(Q - 1)/2$. Therefore, this results in $2Q + (Q - 1)/2$ memory accesses for sparse LBM kernels with the AA streaming

Table 1. Memory accesses per cell for Pull and AA pattern on CPU with size of PDFs $B_{pdf} = 8$ Byte, size of indices in the index-list $B_{idx} = 4$ Byte and $Q = 19$.

Memory accesses CPU		
	Dense data	Sparse data
Pull	$3Q \cdot B_{pdf}$	$3Q \cdot B_{pdf} + (Q - 1) \cdot B_{idx}$
AA	$2Q \cdot B_{pdf}$	$2Q \cdot B_{pdf} + (Q - 1)/2 \cdot B_{idx}$
Reduction (1-AA/Pull)	33.3 %	35.6 %

Table 2. Memory accesses per cell for Pull and AA pattern on GPU with size of PDFs $B_{pdf} = 8$ Byte, size of indices in the index-list $B_{idx} = 4$ Byte and $Q = 19$.

Memory accesses GPU		
	Dense data	Sparse data
Pull pattern	$2Q \cdot B_{pdf}$	$2Q \cdot B_{pdf} + (Q - 1) \cdot B_{idx}$
AA pattern	$2Q \cdot B_{pdf}$	$2Q \cdot B_{pdf} + (Q - 1)/2 \cdot B_{idx}$
Reduction (1-AA/Pull)	0 %	9.7 %

pattern. We see in [Table 1](#) that the AA pattern on a CPU reduces the memory accesses compared to the pull pattern by

$$1 - \frac{3Q \cdot B_{pdf} + (Q - 1) \cdot B_{idx}}{2Q \cdot B_{pdf} + (Q - 1)/2 \cdot B_{idx}}. \quad (10)$$

Because well-optimized LBM codes are usually memory-bound, an increase in the performance of the LBM by the same ratio can be expected.

As already mentioned above, this performance boost can only be achieved on CPUs, as GPUs do not work with similar caches. No "write allocate" on the cache can be avoided. Therefore, only half the memory accesses for the index-list can be saved for the sparse approach, as shown in [Table 2](#).

On the other hand, the condition to store the temporary PDF field can be avoided on CPUs and accelerators. So the memory consumption for the sparse LBM in [Equation 9](#) shrinks to

$$M_{sparse,aa} = N_{cells} \cdot \left(\underbrace{Q \cdot B_{PDF}}_{PDF-list} + \underbrace{(Q - 1) \cdot B_{idx}}_{index-list} + \underbrace{5 \cdot B_{PDF}}_{other\ fields} \right) \cdot \phi. \quad (11)$$

So for a D3Q19 stencil, double precision PDFs, and an integer index-list, we save 36.5% of memory consumption by utilizing the AA streaming pattern for the sparse data structure.

Benchmarking Results In [Figure 8](#) the single GPU benchmarking results for a sparse LBM kernel on a NVIDIA A100 with a D3Q19 stencil and 256^3 lattice cells are presented. We compare the pull streaming pattern with the AA pattern for various collision operators. The theoretical peak performance is calculated by the bandwidth, which is 1367 GB/s found by streaming benchmarks ([Siefert et al. \(2023\)](#)), and the number of theoretical memory accesses from [Table 2](#).

We observe, that the performance of both streaming patterns is close to the theoretical performance for all of the presented collision operators. The average performance increase of the AA pattern compared to the pull pattern on accelerators is $\sim 7.5\%$, which is close to the theoretically

achievable performance increase of 9.7% from [Table 2](#). Therefore, in addition to the avoidance of the storage of the second PDF field, it is also worth to employ the AA pattern on GPUs in terms of performance.

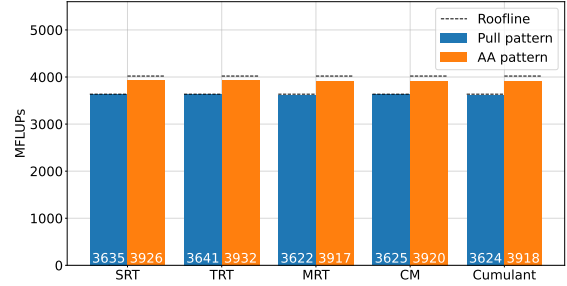


Figure 8. Single GPU Benchmark for pull vs AA streaming pattern for single relaxation time (SRT), two relaxation time (TRT), multi relaxation time (MRT), central moment (CM) and cumulant collision model on a D3Q19 stencil with 256^3 cells on a single NVIDIA A100.

Communication Hiding

Communication hiding is used to overlap communication with computation. For this, the domain on every block has to be divided into a "block interior" and a "frame", as illustrated in [Figure 9](#). The frame only consists of the outermost cells, while the block interior consists of all other cells. An exemplary code to achieve communication hiding is shown in [Algorithm 1](#). At first, the communication is started. Every block packs its outermost PDFs in an MPI buffer and performs a non-blocking MPI-Send to its neighbors. Now, the block interior cells can be updated because the information from neighbour blocks is not needed for these cells. After this step, the algorithm must wait for the communication to complete and write the information of the MPI buffers to the ghost layers. Lastly, with the updated information in the ghost layers, the LBM and boundary kernels can now be executed on the cells of the frame.

With this algorithm, the communication of the simulation can be overlapped with the kernel on the interior, which leads to higher performance because of better scalability on an increasing number of MPI processes. The width of the frame in all three dimensions has to be chosen suitably to achieve best possible performance. A thinner frame width would increase the number of cells in the interior, providing more time to overlap the communication. On the other hand, a small frame width results in small kernels. Especially on GPUs, small kernels can not fully utilize the GPU, which can lead to performance drops. Additionally, consecutive memory access in one dimension is not possible for a thin frame, which can also reduce the simulation's performance.

Communication Hiding for Sparse Data Structures

Implementing communication hiding for a sparse data structure is not straightforward because there is no spatial information for the cells. This means that a cell has no direct information about whether it is inside the block interior or part of the frame. To compensate this, we store two additional index lists, one for the interior and one for the PDFs on the

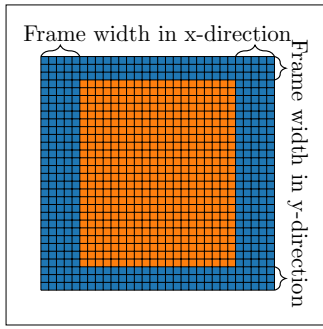


Figure 9. Subdivision of the PDF field in a frame and the block interior to enable communication hiding. In this example, the frame width is 5 in x, and 3 in y-direction.

Algorithm 1 Communication Hiding

- 1: **for** each time step **do**
 - 2: Start communication
 - 3:
 - 4: Run boundary kernels on block interior
 - 5: Run LBM kernel on block interior
 - 6:
 - 7: Wait communication
 - 8:
 - 9: Run boundary kernels on frame
 - 10: Run LBM kernel on frame
-

frame. These index lists are initialized by the flag field at the start of the simulation, where spacial information of cells is still present. Furthermore, the pull index for the center PDF of every fluid cell must be stored. This index is used to get the correct write access for kernels on the interior and frame cells. These modifications on the list structure are integrated into the code generation so that they can be turned on and off and allow generated code to run on different architectures.

Scaling results In [Figure 10](#), the weak scaling of the sparse data structure on the JUWELS Booster HPC cluster is presented. JUWELS Booster is currently place 21 of the Top500 HPC systems (June 2024) and consists of 936 compute nodes, each equipped with 4 NVIDIA A100 GPUs (see [Alvarez \(2021\)](#)).

We tested three versions of the communication. One is without communication hiding, one with the minimum frame size of one cell in every direction, and one with a frame thickness of 32 cells in x direction and one cell in y and z direction. This option is promising, since consecutive memory accesses are still enabled in x-direction, while the frame size is still small enough to allow a good communication overlap. In general, a smaller frame size increases the work of the kernels on the interior cells and, therefore, should increase the effectiveness of the communication hiding. On the other hand, the GPU utilization of the kernels on the frame is quite low for a small frame size, and consecutive memory accesses are not secured.

The version without communication hiding performs best up to one node (4 GPUs), see [Figure 10](#). There the intra-node communication speed is quite high since we can exploit the high bandwidth of NVIDIA GPU-to-GPU connections. However, the performance without

communication deteriorates for more than 4 GPUs when the inter-node communication speed becomes relevant.

The benchmark runs with communication hiding start with worse performance on single node, as the overhead of the kernel call on the frame cells limits the performance. Nevertheless, these versions exhibit excellent scalability for up to 32 GPUs. Beyond 32 GPUs, the performance drops to 83% scaling efficiency on 1024 GPUs. This can possibly be explained by the InfiniBand network architecture of JUWELS Booster, which is implemented as a DragonFly+ network. The drop in performance could be caused by the need for communication between different switch islands of the system when more than 32 GPUs are employed.

In these cases, the size of the frame only has a negligible impact. The two scenarios for communication hiding behave similarly. The smaller frame size of $\langle 1, 1, 1 \rangle$ performs a bit better on more than 128 GPUs. Nevertheless, we see that communication hiding can increase the scaling efficiency of the sparse data structure on up to 1024 NVIDIA A100 GPUs from 63% to 83%.

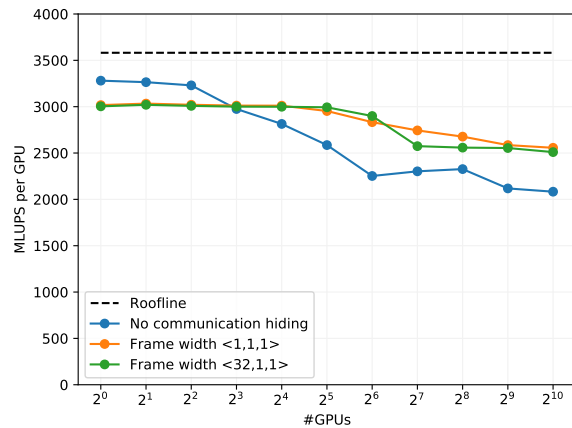


Figure 10. Weak scaling benchmark on NVIDIA A100 GPU cluster JUWELS Booster with different configurations for the communication hiding. The roofline is obtained by a stream benchmark ([Siefert et al. \(2023\)](#)). The runs are executed with 320^3 cells per GPU, with a D3Q19 stencil and SRT collision model on an empty channel setup.

Additionally, we tested the scaling efficiency on the GPU partition of LUMI, which is in the top 5 on the current Top500 list (June 2024). The HPC cluster comprises 2978 nodes with 4 AMDMI250X GPUs per node. Further, every AMD MI250X GPU consists of two Graphical Compute Dices (GCDs) ([Pearson \(2023\)](#)), so we create one MPI process per GCD and show the scaling over the GCDs. As already studied in [Holzer et al. \(2024\)](#), [Lehmann \(2022\)](#) and [Martin et al. \(2023\)](#), it seems not to be possible to achieve significantly better performance than equivalent to approximately 50% of memory bandwidth for LBM codes on a single AMDMI250X. We observe the same behavior in [Figure 11](#).

We tested the three communication routines similar to the benchmarks on JUWELS Booster. For the runs without communication hiding, the scaling behavior is similar as for the larger frame size of $\langle 32, 1, 1 \rangle$. For the cases without communication hiding, we achieve a CDG scaling efficiency

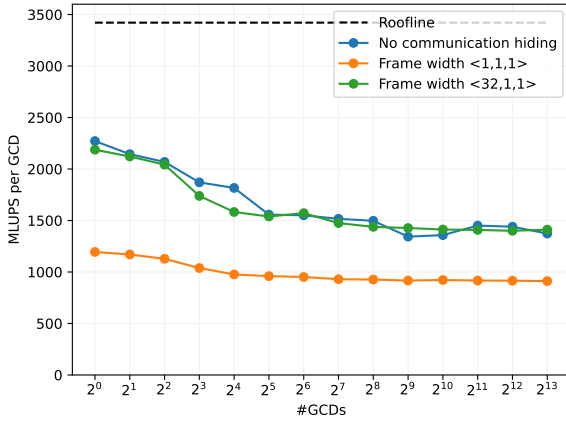


Figure 11. Weak scaling benchmark on GPU cluster LUMI-G with different configurations for the communication hiding. The roofline is obtained by a stream benchmark (Siefert et al. (2023)). The AMD MI250X GPUs have two compute chips per GPU (GCDs). The runs are executed with 256^3 cells per GCD, with a D3Q19 stencil and SRT collision model on an empty channel setup.

of 60% scaling from one to 8192 CDGs (4096 GPUs) and a node (4 GPUs) scaling efficiency of 82%. For the greater frame size $\langle 32, 1, 1 \rangle$ we observe similar scaling behavior as without communication hiding. The expected acceleration and better scaling could not be observed, a finding that should be further investigated in future research. For the small frame size, the scaling efficiency is almost perfect, but the overall performance is much worse than for the other communication strategies. Again this behavior is unexpected. The non-consecutive memory accesses and kernel calls with small execution times could be the reason for the relatively poor overall performance of the simulation in these cases.

Applications

To evaluate the performance of the sparse data structure in a more realistic scenario than the artificial porosity benchmark as in Figure 4 or the weak scaling of an empty channel on JUWELS Booster (Figure 10) and on LUMI (Figure 11), we set up three different applications. The first is a flow through a porous medium consisting of a stationary particle bed. The second one is an extended version of the first application, where the bottom part of the domain consists of the same particle bed, while the upper domain is a free flow, such that we simulate the interaction of a free flow with a porous sediment bed. The last application is the flow through a geometry of coronary arteries, which also results in a complex and sparse domain.

Flow through Porous Media

The efficient simulation of fluid flow through porous media is an ongoing research topic, for example in Pan et al. (2004), Yang et al. (2023), Han and Cundall (2013) or Ambekar et al. (2023), to mention a few. For this porous application, we generated a particle bed with the WALBERLA molecular dynamics module MESA-PD, as shown in Rettinger and

Rüde (2018). We defined a domain of 0.1 meters in every dimension and filled it with 21580 particles with a diameter of 0.0041m. This setup is illustrated in Figure 12 and results in an average porosity of 0.356663.

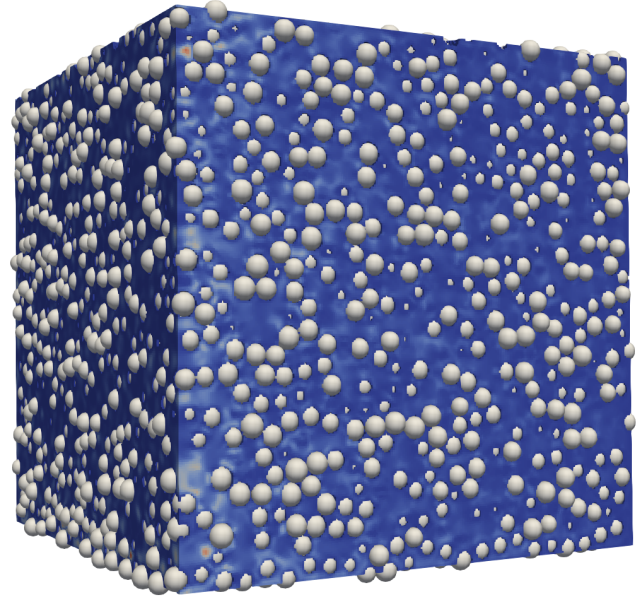


Figure 12. Flow through a particle bed consisting of 21580 particles of 0.0041m diameter, which corresponds to an average porosity of 0.356663. The size of the domain is 0.1m in every dimension.

We decomposed the domain with 64 blocks in a $4 \times 4 \times 4$ arrangement to run on 64 NVIDIA A100 GPUs on JUWELS Booster. While we fixed the number of blocks to 64, we increase the cells per block and therefore also the resolution of the domain and the number of total cells, as shown in Figure 13. We performed this benchmark for the sparse data structure, and compare it to the dense data structure.

We first focus on at the "kernel-only" results in Figure 13, which only run the LBM kernel without handling boundaries or performing communication. We observe, that for block sizes below 64^3 , the GPU utilization is too low to achieve good performance. Both, the sparse and the dense kernel saturate at a block size of 256^3 . Further, we note that the performance of the sparse data structure is approximately two times higher than for the dense structure. This also fits quite well to the results in Figure 4 for a porosity of $\phi \sim 0.35$. The sparse kernel-only performance does not quite reach the theoretical bandwidth limit. This could be caused by some imbalances, since the porosity varies between the blocks, from a minimum of 0.337816 to a maximum of 0.392441. This means, that some blocks, and therefore processes, have more workload in terms of cells. We measure the performance at the end of the simulation run, when all processes finished their work, so the performance is determined by the slowest processor. The performance of the dense kernel on the other side is not affected by the porosity differences, and therefore performs exactly the same work on every MPI process and thus does not suffer from load imbalance issues.

When running the full simulation including boundary handling and communication routines, we again observe low performance for small block sizes, which can be

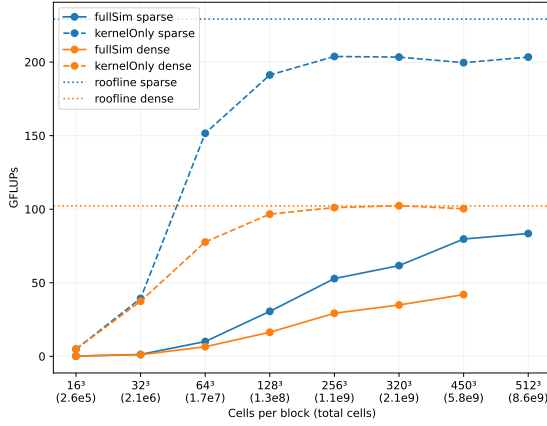


Figure 13. Comparison of the sparse and the dense data structure for the flow through the particle bed in Figure 12. The number of WALBERLA blocks is fixed to 64 while the cells per blocks increases, and therefore also the resolution and the number of total cells increases. The benchmark was executed on 64 NVIDIA A100 GPUs on JUWELS Booster with one block per GPU.

explained by the low utilization of GPUs. However, this time, there is no saturation for a block size of 256^3 because a more extensive block size results in better communication hiding when the ratio between computational work and communication improves in favor of computational work. For the dense structure, it was not possible to perform simulations with a block size of 512^3 , as the memory consumption exceeded the 40 GB of the GPU RAM of a single A100. For the sparse structure, this is not a problem, as for a porosity of 0.356663 we save around 50% of memory compared to the dense structure.

For this application, we significantly benefit from the sparse data structure, as it achieves a performance increase of $\sim 90\%$ compared to the dense one for a block size of 450^3 . For a block size of 512^3 , which results in a cell resolution of 4.8828×10^{-5} m and 8.6×10^9 total cells, it achieves an overall performance of 203.408 GFLUPs for the kernel-only call and 83.475 GFLUPs for the full-simulation run. Further, as shown in Figure 5, for a domain with an average porosity of ~ 0.35 , we are able to save around 50% of memory consumption by utilizing the sparse data structure.

Free Flow over River Bed

The second application is the simulation of a free flow over a river bed similar to Kemmler et al. (2023) or Fattahi et al. (2016). In Figure 14, the bottom part of the domain consists of the same porous medium / particle bed as the first application in Figure 12, with the same average porosity of about ~ 0.35 . The upper part of the domain is a free flow only, so 100% fluid cells in this part of the domain. The average porosity of the domain is ~ 0.68 .

This application is suitable for utilizing the hybrid data structure. As already indicated in Figure 14, the blocks in the upper part of the domain should hold their data in a dense structure (red blocks). In contrast, the blocks in the porous part of the domain should be stored with a sparse data structure (blue blocks). The framework includes the

functionality to select the appropriate data structure for each block, the user only has to specify an appropriate porosity threshold.

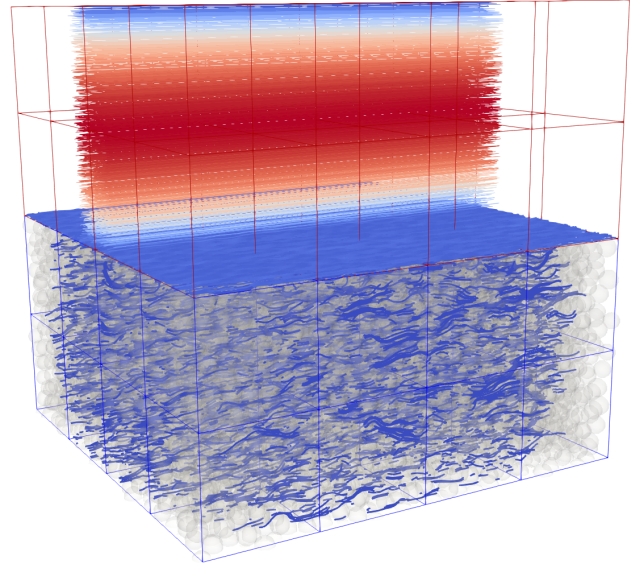


Figure 14. Free Flow over a particle bed. The porosity of the blocks in the particle bed on the bottom (blue blocks) have a porosity of about 0.35, while the upper blocks (red blocks) consists of fluid cells only.

In Figure 15, a comparison of the sparse, the dense and the hybrid data structure is shown. The simulations are again executed on the JUWELS Booster GPU cluster, with a fixed number of NVIDIA A100 GPUs and one MPI process per GPU. The performance of the raw LBM kernel (kernel-only) is plotted, as well as the entire simulation run, including communication between the MPI processes. We fixed the number of GPUs to 64 as well as the problem size to 10^9 cells and only vary the cells per block, resulting in a high number of blocks for small cells per block and one block per GPU for the largest block size of 256^3 cells.

Evaluating the raw kernel performance first, we again observe that a more significant number of cells per block leads to a better utilization of the GPU.

Load-balancing issues can emerge when using a sparse or a hybrid data structure with multiple blocks per GPU. This is because the block partitioning of a domain can lead to a wide span of porosity values on the blocks. When decomposing the river bed simulation in Figure 14 with sparse blocks only, this results in half of the blocks yielding a porosity of ~ 0.35 and the other half yielding a porosity of 1.0. One can calculate the workload of a sparse WALBERLA block on a GPU similar to the number of memory accesses in Table 2 with

$$w_{\text{sparse}} = \underbrace{(2 \cdot Q \cdot B_{\text{PDF}})}_{\text{PDF list read/write}} + \underbrace{(Q - 1) \cdot B_{\text{idx}}}_{\text{Index list read}} \cdot \phi \quad (12)$$

with Q as the stencil size and ϕ as the porosity.

The workload for the dense block on a GPU is

$$w_{\text{dense}} = \underbrace{2 \cdot Q \cdot B_{\text{PDF}}}_{\text{PDF field read/write}}, \quad (13)$$

which is not depending on the porosity of the block.

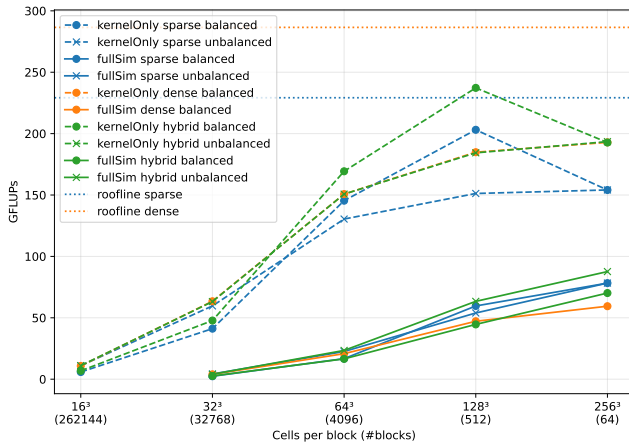


Figure 15. Comparison of the sparse, dense and hybrid data structure for the free flow over a particle bed in Figure 14 on 64 NVIDIA A100 GPUs on Juwels Booster. The problem size is fixed to $1.07 \cdot 10^9$ cells, while the number of cells per block and therefore also the number of blocks vary. The LBM kernel-only performance is shown as well as the performance of the whole simulation including boundary handling and communication between MPI processes.

For the simulation run with sparse data blocks only, the workload of the blocks differs significantly depending on their porosity. Therefore, we employ a load-balancing algorithm to balance the blocks over the MPI processes to reach a better workload distribution. We used a space-filling-Hilbert-curve approach, as described in Schornbaum and Rde (2018).

In Figure 15, we observe that the load-balancing works well for the sparse kernel-only runs. Especially for the block sizes of 64^3 and 128^3 , the load-balancing seems to reduce the workload unbalance significantly and, therefore, increases the performance. For 256^3 cells per block, there is only one block per GPU, so no load-balancing is possible in this case.

No load balancing is necessary for the dense data structure, as every block has the same workload. We see that the kernel-only runs of the dense data structure outperform the unbalanced sparse runs. This is because the sparse data structure is slower than the dense structure on the blocks with a porosity of 1.0 (see again Figure 4), and all MPI processes must wait for the processes holding these blocks. However, when balancing the workload for the sparse kernels, at least for a block size of 128^3 , we can achieve a higher performance than the dense kernels.

The kernel-only runs for the hybrid data structure without load balancing closely follow the results of the dense kernels in Figure 15. Without load balancing, the low performance of the dense blocks in the porous region heavily dominates the runtime. However, here we can balance the workload to achieve better results. So for the kernel-only runs, using the workload-balanced hybrid data outperforms the other kernels for all block sizes. The only exception is for 256^3 cells per block. There no load-balancing is possible, because there is only one block per GPU.

We observe a similar behavior when studying the entire simulation runs in Figure 15. This now includes the communication between the MPI processes. Overall, the sparse data structure performs superior to the dense one on the block sizes of 128^3 and 256^3 cells per block.

Table 3. Workload per MPI process / GPU before and after load balancing for the hybrid data structure run with 128^3 cells per block in Figure 15.

Workload	Average	Std deviation	Min	Max
Unbalanced	1757.47	675.194	1038	2432
Balanced	1757.47	102.644	1520	1826

For the hybrid structure, we observe unexpected behavior. Here, the load-balanced simulation performs worse than the sparse simulations, while the unbalanced hybrid simulation reaches the highest MFLUPs values of all tested data structures. In Table 3, the workload per MPI process of the simulation with the hybrid data structure for 128^3 cells per block is presented. We observe that the standard deviation of the average workload is significantly lower than for the unbalanced execution. Still, the performance of the balanced run is worse for the full-simulation. Here we observe that the load-balancing algorithm successfully distributes the workload over the MPI processes but it reduces the spatial locality of the blocks with respect to each other. Therefore, the communication is more expensive.

Nevertheless, for a complex domain setup such as a free flow over a riverbed, we also manage to improve the application’s performance by utilizing the sparse or the hybrid data structure. Additionally, we note the reduced memory consumption as presented in Figure 5. Overall, when half of the domain consists of a porous medium, such as in Figure 14, we save about 25% of memory with the hybrid data structure.

Coronary Artery

Finally, we present performance results for the flow in a coronary artery. This is a topic of high interest in medical engineering and has been studied, for example, in Axner et al. (2009), Afrouzi et al. (2020), Bernaschi et al. (2010) and Godenschwager et al. (2013). The flow in a coronary artery results in a complex and highly sparse domain. An example setup for this application is shown in Figure 16. While the whole domain would consist of a very high number of blocks, we can discard all blocks that do not contain fluid cells. Still, the remaining blocks have a very low porosity. Of course, when lowering the size of the block, the block structure would converge better to the geometry and result in higher block porosities. However, small block sizes also lead to under-utilization of GPUs, as already shown in Figure 13.

In Figure 17, we compare the performance of the sparse and the dense data structure on JUWELS Booster. We fixed the number of NVIDIA A100 GPUs to 60 and the problem size to $1.2 \cdot 10^8$ fluid cells while varying the block size and, therefore, also the number of blocks. Again, we observe the behavior of a small block size, which results in low performance for the kernel-only runs of the sparse data structure. We experience that increasing the block size up to 128^3 cells per block leads to higher performance of the raw sparse LBM kernel. For block sizes larger than 128^3 , the porosity drops below $\phi < 0.1$. We observe in Figure 4 that the sparse LBM performance starts to deteriorate for a porosity smaller than 0.1. Therefore, for block sizes larger 128^3 , the performance of the sparse kernel in Figure 17 shrinks because of the low block porosities. The sweet spot

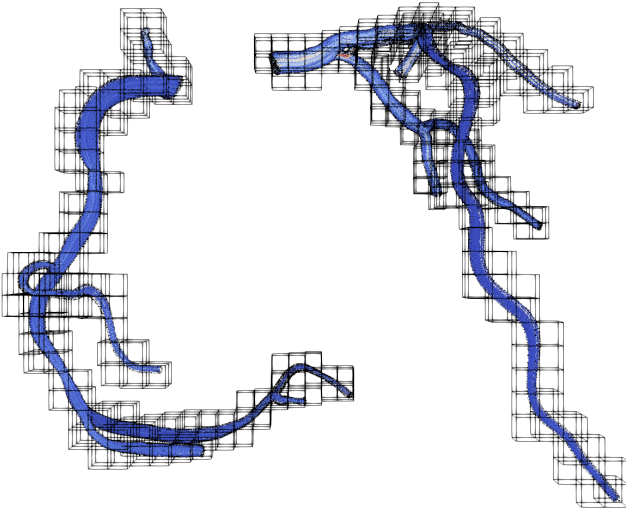


Figure 16. Domain partitioning of a coronary artery with $1.2 \cdot 10^8$ fluid cells, 531 blocks and 128^3 cells per block.

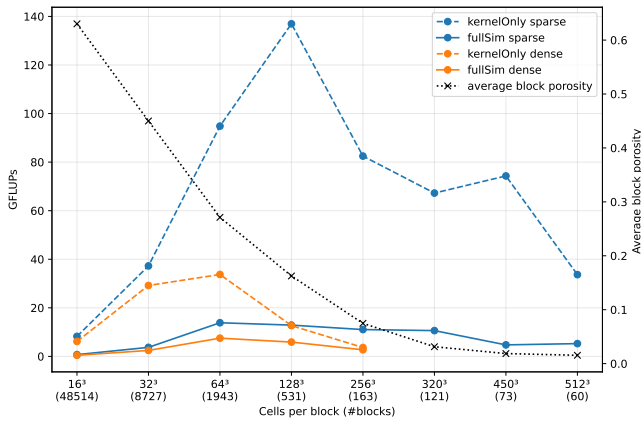


Figure 17. Comparison of the sparse and the dense data structure for the artery flow in Figure 16 on 60 NVIDIA A100 GPUs on JUWELS Booster. The problem size is fixed to a number of $1.2 \cdot 10^8$ fluid cells, while the block size and therefore also the number of blocks varies.

between large block sizes for good GPU utilization and a porosity greater than 0.1 for good kernel performance is a block size of 128^3 cells per block for this setup. The same behavior does not emerge for the sparse full simulations. Here, the performance is relatively stable for moderate block sizes. This is because the performance is heavily dominated by communication, which is especially high in this application because of the high number of blocks per MPI process.

Nevertheless, the sparse data structure shows significantly higher performance than the dense data structure for all block sizes. This is true for the kernel-only runs and the full simulation runs. For a block size of 128^3 cells, we achieve a speed-up of about 11 for the kernel-only run and still a speed up of 2 for the full simulation.

Also remarkable is the amount of memory we can save for the artery setup. So when choosing a block size of 128^3 cells per block to reach maximum raw performance; then, we end up with an average block porosity of $\phi \sim 0.16$. This means that according to Figure 5, we save about 75% of memory when using the sparse instead of the dense data structure.

We were not able to acquire results for the dense structure for block sizes greater than 256^3 because the NVIDIA A100 RAM ran out of memory.

Parts of this work are comparable to Martin et al. (2023). In this article, the framework HARVEY is ported to different programming models such as CUDA, HIP, SYCL and Kokkos. The authors compare the performance on different hardware, among others also on NVIDIA A100 and AMD MI250X GPUs. HARVEY is a LBM based CFD software with a focus on simulations of blood flow in patient-derived aortas, also utilizing the indirect addressing approach.

Martin et al. (2023) measure the performance of HARVEY and a proxy app for NVIDIA A100 GPUs on the HPC System Polaris⁶. Their proxy app is used to show the maximum achievable performance for simple test cases. Their results of the proxy app for an empty channel flow on one node (4 NVIDIA A100 GPUs) reaches around 12000 MLUPS, equivalent to 3000 MLUPS per A100 GPU. This is close to what we achieve, as shown in Figure 10 for the communication-hiding cases. The actual HARVEY framework performs slightly worse for the same empty channel with around 2250 MLUPS per GPU. On the maximum scaling size of 1024 NVIDIA A100 GPUs, the proxy-app reaches around 10^4 MLUPS, equivalent to 976 MLUPS per GPU. The HARVEY framework achieves around $6 \cdot 10^4$ MLUPS, equivalent to 585 MLUPS per A100 GPU. In Figure 10 WALBERLA achieves 2500 MLUPS per GPU on 1024 NVIDIA A100 GPUs. We conclude that the scaling efficiency of WALBERLA seems to be superior. The results may not be fully comparable, as the team of Martin et al. (2023) performs a piece-wise strong-scaling, while we show the weak scaling of our software. Further, they operated on a different HPC cluster, so especially the scaling performance can depend significantly on the configuration of the HPC system.

When comparing the results for the artery geometry with a resolution of $55 \mu\text{m}$, HARVEY achieves around $4 \cdot 10^4$ MLUPS for 64 A100 GPUs, so 625 MLUPS per GPU. In Figure 17 WALBERLA was able to achieve 1374 MLUPS per GPU for the kernel-only runs, but only 230 MLUPS for the full simulation performance. Of course, the underlying geometry of the artery is different, so again the results may not be fully comparable. Nevertheless, there is still room to optimize the WALBERLA framework in terms of load-balancing and communication-efficiency, especially for cases with multiple blocks per GPU.

Further, Martin et al. (2023) show comparable results on the AMD MI250X GPUs, which were tested on the Frontier⁷ HPC system. We compare the results for 4 GCDs. The proxy app of shows around 2250 MLUPS per GCD, while WALBERLA shows 2100 MLUPS per GCD (see Figure 11). So also the team of Martin et al. (2023) confirm, that LBM algorithms are not able to achieve more than 60% of the maximum theoretical performance of the AMD MI250X GPUs. For 1024 CDGs, the proxy app shows a performance of around 10^6 MLUPS, so 976 MLUPS per CDG. WALBERLA was able to achieve 1500 MLUPS per GCD on the same number of GCDs, so it shows a slightly better scaling efficiency. Again, the results are not fully comparable, as we compare a weak scaling with a piece-wise strong-scaling and also run on different systems.

Conclusion

In this article, we presented the benefit of sparse LBM kernels, especially when using accelerator cards. We compared the sparse and the dense data structure on a single GPU and found that for a domain porosity of < 0.8 , the sparse data structure outperforms the dense data structure in terms of performance and memory consumption.

The sparse kernels show excellent performance for the pull streaming pattern for various collision operators such as single-/two-/multi-relaxation times, central moments, or cumulants on a single GPU. We managed to further increase the performance by $\sim 7.5\%$ and reduce the memory consumption by 36.5% by utilizing an AA streaming pattern on GPUs. We were also able to show a scaling efficiency of the sparse data structure of over 82% on the JUWELS Booster and LUMI-G HPC system for 1024 and 4096 GPUs, respectively.

We set up a porous media flow simulation and achieved a speed-up of 1.9 and reduced the memory consumption by 50% . For an artery blood flow simulation, we gained a speed-up of 2 dependent on the block sizes and achieved a decrease of memory consumption of about 75% . We experienced imbalances in the distribution of the work over the MPI processes when using the sparse data structures. To maximize the efficiency of the sparse LBM, we employed load balancing, but more research is needed to fully optimize the workload distribution while maintaining the spatial locality of the neighboring blocks.

To further increase the flexibility of the code generation with *lbmpy*, future work is planned to support the emerging INTEL GPUs by having a SYCL⁸ back-end. As SYCL is available on most currently available systems, the code generation could be used to generate optimized sparse LB kernels for all existing and upcoming hardware such as CPU, accelerator cards, or even exotic hardware such as Accelerated Processing Units (APUs) or Field Programmable Gate Arrays (FPGAs).

Acknowledgements

This work was supported by the SCALABLE project (www.scalable-hpc.eu/). This project has received funding from the European High-Performance Computing Joint Undertaking (JU) under grant agreement No 956000. The JU receives support from the European Union's Horizon 2020 research and innovation program and France, Germany, and the Czech Republic. The authors gratefully acknowledge the Gauss Centre for Supercomputing e.V. (www.gauss-centre.eu/) for funding this project by providing computing time through the John von Neumann Institute for Computing (NIC) on the GCS Supercomputer JUWELS at Jülich Supercomputing Centre (JSC). We acknowledge the EuroHPC Joint Undertaking for awarding this project access to the EuroHPC supercomputer LUMI, hosted by CSC (Finland) and the LUMI consortium through a EuroHPC Regular Access call. The authors gratefully acknowledge the scientific support and HPC resources provided by the Erlangen National High Performance Computing Center (NHR@FAU) of the Friedrich-Alexander-Universität Erlangen-Nürnberg (FAU).

Notes

1. Top500 List: <https://www.top500.org/>, accessed: 2024-6-3
2. LUMI Supercomputer: <https://www.lumi-supercomputer.eu/>, accessed: 2024-3-13
3. HIP: <https://rocm.docs.amd.com/projects/HIP/en/latest/>, accessed: 2024-5-13
4. CUDA: <https://developer.nvidia.com/cuda-toolkit>, accessed: 2024-5-13
5. IPython: <https://ipython.org/>, accessed: 2024-4-15
6. Polaris: <https://www.alcf.anl.gov/polaris>, accessed: 2024-8-2
7. Frontier: <https://www.olcf.ornl.gov/olcf-resources/compute-systems/frontier/>, accessed: 2024-8-2
8. SYCL: <https://www.khronos.org/sycl/>, accessed: 2024-04-16

References

- Afrouzi HH, Ahmadian M, Hosseini M, Arasteh H, Toghraie D and Rostami S (2020) Simulation of blood flow in arteries with aneurysm: Lattice Boltzmann Approach (LBM). *Computer Methods and Programs in Biomedicine* 187: 105312. DOI: 10.1016/j.cmpb.2019.105312.
- Alvarez D (2021) Jewels cluster and booster: Exascale pathfinder with modular supercomputing architecture at Jülich supercomputing centre. *Journal of large-scale research facilities JLSRF* 7. DOI:10.17815/jlsrf-7-183.
- Ambekar AS, Schwarzmeier C, Rüde U and Buwa VV (2023) Particle-resolved turbulent flow in a packed bed: RANS, LES, and DNS simulations. *AIChE Journal* 69(1). DOI:10.1002/aic.17615.
- Axner L, Hoekstra AG, Jeays A, Lawford P, Hose R and Sloot PM (2009) Simulations of time harmonic blood flow in the Mesenteric artery: Comparing finite element and lattice Boltzmann methods. *BioMedical Engineering OnLine* 8(1): 23. DOI:10.1186/1475-925X-8-23.
- Bailey P, Myre J, Walsh SD, Lilja DJ and Saar MO (2009) Accelerating Lattice Boltzmann Fluid Flow Simulations Using Graphics Processors. In: *2009 International Conference on Parallel Processing*. pp. 550–557. DOI:10.1109/ICPP.2009.38.
- Bauer M, Eibl S, Godenschwager C, Kohl N, Kuron M, Rettinger C, Schornbaum F, Schwarzmeier C, Thönnies D, Köstler H and Rüde U (2020) walberla: A block-structured high-performance framework for multiphysics simulations. DOI: 10.1016/j.camwa.2020.01.007.
- Bauer M, Hötzer J, Ernst D, Hammer J, Seiz M, Hierl H, Hönig J, Köstler H, Wellein G, Nestler B and Rüde U (2019) Code generation for massively parallel phase-field simulations. Association for Computing Machinery. DOI:10.1145/3295500.3356186.
- Bauer M, Köstler H and Rüde U (2021) lbmpy: Automatic code generation for efficient parallel lattice Boltzmann methods. *Journal of Computational Science* 49: 101269. DOI:10.1016/j.jocs.2020.101269.
- Bernaschi M, Fatica M, Melchionna S, Succi S and Kaxiras E (2010) A flexible high-performance Lattice Boltzmann GPU code for the simulations of fluid flows in complex geometries. *Concurrency and Computation: Practice and Experience* 22(1): 1–14. DOI:10.1002/cpe.1466.

- Bernaschi M, Succi S, Fyta M, Kaxiras E, Melchionna S and Sircar JK (2008) MUPHY: A parallel high performance MULTI PHYSics/Scale code. In: *2008 IEEE International Symposium on Parallel and Distributed Processing*. pp. 1–8. DOI:10.1109/IPDPS.2008.4536464.
- Brodtkorb AR, Hagen TR and Sætra ML (2013) Graphics processing unit (GPU) programming strategies and trends in GPU computing. *Journal of Parallel and Distributed Computing* 73(1): 4–13. DOI:10.1016/j.jpdc.2012.04.003.
- Chen S and Doolen GD (1998) Lattice Boltzmann method for fluid flows. *Annual Review of Fluid Mechanics* 30(1): 329–364. DOI:10.1146/annurev.fluid.30.1.329.
- Fattahi E, Waluga C, Wohlmuth B and Rüde U (2016) Large Scale Lattice Boltzmann Simulation for the Coupling of Free and Porous Media Flow. In: Kozubek T, Blaheta R, Šístek J, Rozložník M and Čermák M (eds.) *High Performance Computing in Science and Engineering*, volume 9611. Cham: Springer International Publishing. ISBN 978-3-319-40360-1 978-3-319-40361-8, pp. 1–18. DOI:10.1007/978-3-319-40361-8_1.
- Geier M, Schönherr M, Pasquali A and Krafczyk M (2015) The cumulant lattice Boltzmann equation in three dimensions: Theory and validation. *Computers & Mathematics with Applications* 70(4): 507–547. DOI:10.1016/j.camwa.2015.05.001.
- Godenschwager C, Schornbaum F, Bauer M, Köstler H and Rüde U (2013) A framework for hybrid parallel flow simulations with a trillion cells in complex geometries. In: *Proceedings of the International Conference on High Performance Computing, Networking, Storage and Analysis*, SC '13. New York, NY, USA: Association for Computing Machinery. ISBN 978-1-4503-2378-9, pp. 1–12. DOI:10.1145/2503210.2503273.
- Han Y and Cundall PA (2013) LBM–DEM modeling of fluid–solid interaction in porous media. *International Journal for Numerical and Analytical Methods in Geomechanics* 37(10): 1391–1407. DOI:10.1002/nag.2096.
- Hasert M, Masilamani K, Zimny S, Klimach H, Qi J, Bernsdorf J and Roller S (2014) Complex fluid simulations with the parallel tree-based Lattice Boltzmann solver Musubi. *Journal of Computational Science* 5(5): 784–794. DOI:10.1016/j.jocs.2013.11.001.
- Hennig F, Holzer M and Rüde U (2022) Advanced Automatic Code Generation for Multiple Relaxation-Time Lattice Boltzmann Methods. DOI:10.48550/arXiv.2211.02435.
- Hijma P, Heldens S, Sclocco A, van Werkhoven B and Bal HE (2023) Optimization Techniques for GPU Programming. *ACM Computing Surveys* 55(11): 239:1–239:81. DOI:10.1145/3570638.
- Holzer M, Mitchell T, Leonardi CR and Ruede U (2024) Development of a central-moment phase-field lattice Boltzmann model for thermocapillary flows: Droplet capture and computational performance.
- Kemmler S, Schwarzmeier C, Rettinger C, Plewinski J, Núñez-González F, Köstler H, Rüde U and Vowinkel B (2023) Geometrically Resolved Simulation of Upstream Migrating Antidune Formation and Propagation. In: *40th IAHR World Congress*.
- Krüger T, Kusumaatmaja H, Kuzmin A, Shardt O, Silva G and Viggen EM (2017) *The Lattice Boltzmann Method*. Springer International Publishing. DOI:10.1007/978-3-319-44649-3.
- Kummerländer A, Dorn M, Frank M and Krause MJ (2023) Implicit propagation of directly addressed grids in lattice Boltzmann methods. *Concurrency and Computation: Practice and Experience* DOI:10.1002/cpe.7509.
- Lai J, Yu H, Tian Z and Li H (2020) Hybrid MPI and CUDA Parallelization for CFD Applications on Multi-GPU HPC Clusters. *Scientific Programming* 2020: e8862123. DOI: 10.1155/2020/8862123.
- Latt J, Malaspinas O, Kontaxakis D, Parmigiani A, Lagrava D, Brogi F, Belgacem MB, Thorimbert Y, Leclaire S, Li S, Marson F, Lemus J, Kotsalos C, Conradin R, Coreixas C, Petkantchin R, Raynaud F, Beny J and Chopard B (2021) Palabos: Parallel Lattice Boltzmann Solver. *Computers & Mathematics with Applications* 81: 334–350. DOI:10.1016/j.camwa.2020.03.022.
- Lehmann M (2022) Esoteric Pull and Esoteric Push: Two Simple In-Place Streaming Schemes for the Lattice Boltzmann Method on GPUs. *Computation* 10(6): 92. DOI:10.3390/computation10060092.
- Lehmann M, Krause MJ, Amati G, Sega M, Harting J and Gekle S (2022) On the accuracy and performance of the lattice Boltzmann method with 64-bit, 32-bit and novel 16-bit number formats. *Physical Review E* 106(1): 015308. DOI:10.1103/PhysRevE.106.015308.
- Liu Z, Chu X, Lv X, Liu H, Fu H and Yang G (2023) Accelerating Large-Scale CFD Simulations with Lattice Boltzmann Method on a 40-Million-Core Sunway Supercomputer. In: *Proceedings of the 52nd International Conference on Parallel Processing*. Salt Lake City UT USA: ACM. ISBN 9798400708435, pp. 797–806. DOI:10.1145/3605573.3605605.
- Martin A, Liu G, Ladd W, Lee S, Gounley J, Vetter J, Patel S, Rizzi S, Mateevitsi V, Insley J and Randles A (2023) Performance Evaluation of Heterogeneous GPU Programming Frameworks for Hemodynamic Simulations. In: *Proceedings of the SC '23 Workshops of The International Conference on High Performance Computing, Network, Storage, and Analysis*. Denver CO USA: ACM. ISBN 9798400707858, pp. 1126–1137. DOI:10.1145/3624062.3624188.
- Mattila K, Puurtinen T, Hyväluoma J, Surmas R, Myllys M, Turpeinen T, Robertsén F, Westerholm J and Timonen J (2016) A prospect for computing in porous materials research: Very large fluid flow simulations. *Journal of Computational Science* 12: 62–76. DOI:10.1016/j.jocs.2015.11.013.
- Pan C, Prins JF and Miller CT (2004) A high-performance lattice Boltzmann implementation to model flow in porous media. *Computer Physics Communications* 158(2): 89–105. DOI: 10.1016/j.cpc.2003.12.003.
- Pearson C (2023) Interconnect Bandwidth Heterogeneity on AMD MI250x and Infinity Fabric.
- Rak T (2024) Parallel Programming in the Hybrid Model on the HPC Clusters. In: Malhotra R, Sumalatha L, Yassin SMW, Patgiri R and Muppalaneni NB (eds.) *High Performance Computing, Smart Devices and Networks*. Singapore: Springer Nature. ISBN 978-981-9966-90-5, pp. 207–219. DOI:10.1007/978-981-99-6690-5_15.
- Randles A, Draeger EW, Ooppelstrup T, Krauss L and Gunnels JA (2015) Massively parallel models of the human circulatory system. In: *Proceedings of the International Conference for High Performance Computing, Networking, Storage and Analysis*, SC '15. New York, NY, USA: Association for

- Computing Machinery. ISBN 978-1-4503-3723-6, pp. 1–11. DOI:10.1145/2807591.2807676.
- Randles AP, Kale V, Hammond J, Gropp W and Kaxiras E (2013) Performance Analysis of the Lattice Boltzmann Model Beyond Navier-Stokes. In: *2013 IEEE 27th International Symposium on Parallel and Distributed Processing*. Cambridge, MA, USA: IEEE. ISBN 978-1-4673-6066-1 978-0-7695-4971-2, pp. 1063–1074. DOI:10.1109/IPDPS.2013.109.
- Rettinger C and Rüde U (2018) A coupled lattice Boltzmann method and discrete element method for discrete particle simulations of particulate flows. *Computers & Fluids* 172: 706–719. DOI:10.1016/j.compfluid.2018.01.023.
- Schorndorf F and Rüde U (2016) Massively Parallel Algorithms for the Lattice Boltzmann Method on Non-uniform Grids. *SIAM Journal on Scientific Computing* 38(2): C96–C126. DOI: 10.1137/15M1035240.
- Schorndorf F and Rüde U (2018) Extreme-Scale Block-Structured Adaptive Mesh Refinement. *SIAM Journal on Scientific Computing* 40(3): C358–C387. DOI:10.1137/17M1128411.
- Schulz M, Krafczyk M, Tölke J and Rank E (2002) Parallelization Strategies and Efficiency of CFD Computations in Complex Geometries Using Lattice Boltzmann Methods on High-Performance Computers. In: Griebel M, Keyes DE, Nieminen RM, Roose D, Schlick T, Breuer M, Durst F and Zenger C (eds.) *High Performance Scientific And Engineering Computing*, volume 21. Berlin, Heidelberg: Springer Berlin Heidelberg. ISBN 978-3-540-42946-3 978-3-642-55919-8, pp. 115–122. DOI:10.1007/978-3-642-55919-8_13.
- Siefert CM, Pearson C, Olivier SL, Prokopenko A, Hu J and Fuller TJ (2023) Latency and Bandwidth Microbenchmarks of US Department of Energy Systems in the June 2023 Top 500 List. In: *Proceedings of the SC '23 Workshops of The International Conference on High Performance Computing, Network, Storage, and Analysis*. Denver CO USA: ACM. ISBN 9798400707858, pp. 1298–1305. DOI:10.1145/3624062.3624203.
- Spinelli GG, Horstmann T, Masilamani K, Soni MM, Klimach H, Stück A and Roller S (2023) HPC performance study of different collision models using the Lattice Boltzmann solver Musubi. *Computers & Fluids* 255: 105833. DOI:10.1016/j.compfluid.2023.105833.
- Vidal D, Roy R and Bertrand F (2010) On improving the performance of large parallel lattice Boltzmann flow simulations in heterogeneous porous media. *Computers & Fluids* 39(2): 324–337. DOI:10.1016/j.compfluid.2009.09.011.
- Wang J, Zhang X, Bengough AG and Crawford JW (2005) Domain-decomposition method for parallel lattice Boltzmann simulation of incompressible flow in porous media. *Physical Review E* 72(1): 016706. DOI:10.1103/PhysRevE.72.016706.
- Watanabe S and Hu C (2022) Performance Evaluation of Lattice Boltzmann Method for Fluid Simulation on A64FX Processor and Supercomputer Fugaku. In: *International Conference on High Performance Computing in Asia-Pacific Region*. Virtual Event Japan: ACM. ISBN 978-1-4503-8498-8, pp. 1–9. DOI: 10.1145/3492805.3492811.
- Wittmann M, Zeiser T, Hager G and Wellein G (2013) Comparison of different propagation steps for lattice Boltzmann methods. *Computers & Mathematics with Applications* 65(6): 924–935. DOI:10.1016/j.camwa.2012.05.002.
- Yang G, Chen Y, Chen S and Wang M (2023) Implementation of a direct-addressing based lattice Boltzmann GPU solver for multiphase flow in porous media. *Computer Physics Communications* 291: 108828. DOI:10.1016/j.cpc.2023.108828.
- Zeiser T, Hager G and Wellein G (2009) Benchmark analysis and application results for lattice Boltzmann simulations on NEC SX vector and Intel Nehalem systems. *Parallel Processing Letters* 19(04): 491–511. DOI:10.1142/S0129626409000389.